

SUPPORTING INFORMATION

Ultra-low Lattice Thermal Conductivity and High Thermoelectric Performance in Chiral-phonon Protected Heterostructures

Jipin Peter¹, Tanu Choudhary¹, Raju K Biswas^{1,2*}

¹*Department of Physics, Faculty of Natural Sciences,*

M S Ramaiah University of Applied Sciences, Bengaluru 560058, India,

²*Department of Physics, North Eastern Regional Institute of Science and Technology, Nirjuli, Arunachal Pradesh – 791109, India*

**E-mail: rkb@nerist.ac.in*

Table S1. Lattice parameters ($a = b$), and bond length (d) of MoSe₂/WSe₂ and MoSeTe/WSeTe heterostructures.

System	Lattice parameter, $a = b$ (Å)	Bond length, d (Å)
MoSe ₂ ¹	3.32	2.54 (Mo – Se)
WSe ₂ ¹	3.32	2.55 (W – Se)
MoSe ₂ /WSe ₂ HS	3.32	2.54 (Mo – Se) 2.54 (W – Se)
MoSeTe/WSeTe HS	3.46	2.56 (Mo – Se) 2.73 (Mo – Te) 2.56 (W – Se) 2.73 (W – Te)

1. Stability

To assess the stability of the studied heterostructures, we calculate the binding energy per atom using the total energies of the heterostructures and the two isolated monolayer system given

as^{2,3},
$$E_{BE/atom} = \left[E_{HS} - \sum_i E_{i,ML} \right] / n_{tot}$$
, where E_{HS} represents the total energy of the heterostructure, while $E_{i,ML}$ and n_{tot} denote the total energy of the constituent monolayer i required to form the heterostructure and number of atoms in the unit cell, respectively. Binding energies are typically expressed as negative values, indicating the chemical synthesizability of the material.² The calculated binding energy per atom suggests that both heterostructures are energetically favourable to form. The MoSe₂/WSe₂ heterostructure (-0.34 eV/atom) exhibits a higher negative binding energy, suggesting greater chemical stability than the MoSeTe/WSeTe

HS (-0.09 eV/atom). Moreover, the computed binding energy value of MoSe₂/WSe₂ heterostructure, are consistent with the previously reported data².

The elastic constants of crystalline solids contribute to the understanding of bonding strength, mechanical property and stability. Furthermore, to shed light into the mechanical stability of MoSe₂/WSe₂ and MoSeTe/WSeTe heterostructures, we compute the stress-strain coefficients, namely the elastic constants C_{ij} . The elastic constant obtained under the PBE method are shown in Table S2. Because of the presence of hexagonal symmetry, the elastic tensor has three independent constants C_{11} , C_{12} , $C_{66} = (C_{11} - C_{12})/2$ and the calculated values of elastic constants satisfy the Born criteria of elastic stability⁴ given as, $C_{11} > 0$, $C_{66} > 0$, indicating the mechanical stability under ambient conditions. Moreover, we utilize the Hill approximation⁵ with elastic constant to evaluate the Young's modulus (Y), bulk modulus (B) and shear Modulus (G) or C_{66} derived by the relation,^{6,7} $Y = (C_{11}^2 - C_{12}^2)/C_{11}$, $B = (C_{11} + C_{12})/2$, and $G = (C_{11} - C_{12})/2$ respectively, for both heterostructures and the respective values are presented in Table S2. The computed moduli values of MoSe₂/WSe₂ heterostructure is higher than those previously reported for the parent materials⁶, indicating their significantly higher structural integrity compared to the monolayer counterparts. The evaluated values of Y , B and G increases continuously from MoSe₂/WSe₂ to MoSeTe/WSeTe heterostructure, indicating a hardening of interatomic interaction forces and higher mechanical stability. To further assess the elastic nature of the studied heterostructures, we evaluate the Pugh ratio (R)⁸, expressed as, $R = B/G$, with the corresponding values presented in Table S2. Notably, the substitution of Te slightly increases the R value (from 1.04 to 1.19), showing an increment of 14.4%, suggesting the enhanced stiffness of MoSeTe/WSeTe structure compared to MoSe₂/WSe₂ HS.

Table S2. Elastic constant values (C_{ij}), Young's modulus (Y), bulk modulus (B), shear modulus (G) and Pugh ratio (R) for MoSe₂/WSe₂ and MoSeTe/WSeTe heterostructures.

System	C_{11} (Nm ⁻¹)	C_{12} (Nm ⁻¹)	Y (Nm ⁻¹)	B (Nm ⁻¹)	G or C_{66} (Nm ⁻¹)	R
MoSe ₂ ⁶	106.90	25.60	103.90	66.25	40.65	1.62
WSe ₂ ⁶	120.40	23.01	116	71.70	48.69	1.47
MoSe ₂ /WSe ₂	850.53	20.72	850.02	435.62	414.90	1.04
MoSeTe/WSeTe	1600.02	12.65	1587.36	871.17	728.85	1.19

To further explore the underlying bonding characteristics in both heterostructures, we have carried out a comprehensive study on Bader charges⁹ for each atomic species and the corresponding values are given in Table S3 of the SI. Notably, the computed Bader charges

indicate that as the size of chalcogen atom increases (from smaller Se to larger Te atom), a steady decline in the charge transfer occurs specifically between the metal and Te atoms. Such low charge transfer observed particularly between the atoms (Mo – Te and W – Te) in MoSeTe/WSeTe compared to MoSe₂/WSe₂ HS, indicates the weakening of ionic bond strength in the system.¹⁰ Moreover, we have investigated chemical bonding integrity of different atoms or atomic groups by performing the crystal orbital Hamilton population (COHP) analysis as a function of energy (E) near the Fermi level for both MoSe₂/WSe₂ and MoSeTe/WSeTe heterostructures, as depicted in Fig. S1. In COHP plot, the positive values indicate antibonding interactions, while, negative values correspond to strong bonding interactions. Interestingly, MoSe₂/WSe₂ HS exhibits prevailed antibonding nature (reaching a maximum value of ~ 0.25) for all the bonds, as clearly visible below the Fermi level as evident in Fig. S1a. However, the incorporation of Te in MoSeTe/WSeTe HS has monotonously increased the antibonding behaviour of Mo/W – Se bonds reaching as high as ~ 0.5 (almost two times higher compared to those in MoSe₂/WSe₂ HS), indicating the weakening of bond strength within the MoSeTe/WSeTe heterostructure, as shown in Fig. S1b of the SI. Moreover, the computed ICOBI values (shown in Table S4 of the Supporting Information) for all the bonds between metal and chalcogen atoms in both heterostructures are in the near proximity of ~ 0.65 . These results reveal the coexistence of both covalent and ionic character, indicating the presence of chemical bonding hierarchy¹¹ in both heterostructures. The aforementioned weakening of chemical bond along with the presence of bonding hierarchy can substantially modulate both phonon and electron transport in the heterostructures.^{10,11}

Table S3. Bader charges for each element [represented in bracket] in MoSe₂/WSe₂ and MoSeTe/WSeTe heterostructures. Additionally, the metal atom to which Se and Te atoms are connected are also mentioned in the bracket.

MoSe ₂ /WSe ₂ HS	MoSeTe/WSeTe HS
+0.88 [Mo]	+0.72 [Mo]
+1.04 [W]	+0.84 [W]
-0.54 [Se (W)]	-0.57 [Se (W)]
-0.45 [Se (Mo)]	-0.45 [Se (Mo)]
-0.42 [Se (Mo)]	-0.26 [Te (Mo)]
-0.49 [Se (W)]	-0.25 [Te (W)]

Table S4. Integrated crystal orbital bond index (ICOBI) values for each bond in MoSe₂/WSe₂ and MoSeTe/WSeTe heterostructures. Here, Se1 and Se2 correspond to different Se atom connecting with Mo as well as W of MoSe₂/WSe₂ heterostructure.

MoSe ₂ /WSe ₂ HS	MoSeTe/WSeTe HS
--	-----------------

0.63 [Mo - Se1]	0.63 [Mo - Se]
0.64 [Mo - Se2]	0.62 [Mo - Te]
0.62 [W - Se1]	0.62 [W - Se]
0.63 [W - Se2]	0.62 [W - Te]

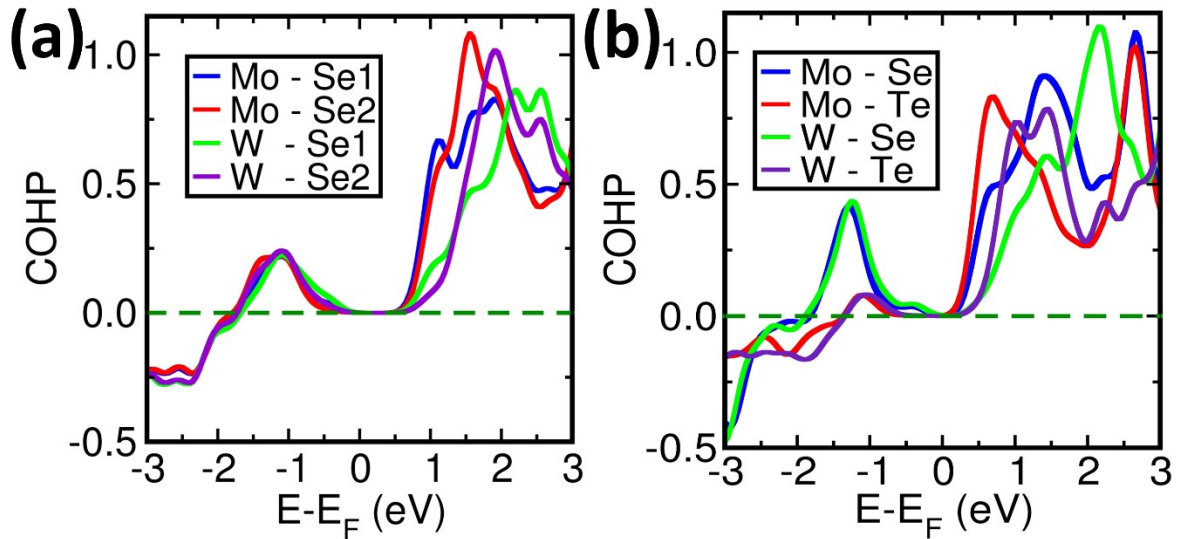


Fig. S1 Crystal orbital Hamilton population (COHP) plot as a function of energy (E) to discern bonding characteristics between different pairs of atoms for (a) $\text{MoSe}_2/\text{WSe}_2$ and (b) $\text{MoSeTe}/\text{WSeTe}$ heterostructures.

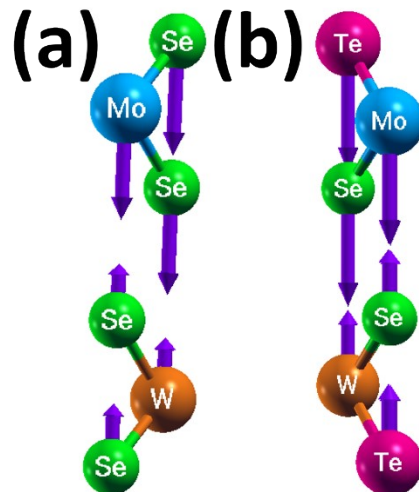


Fig. S2 Eigen vectors of low-lying ZO mode for (a) $\text{MoSe}_2/\text{WSe}_2$ and (b) $\text{MoSeTe}/\text{WSeTe}$ heterostructures, respectively, at high symmetry Γ point, depicting the proximity of MoSe_2 sub-layer limiting the vibration of WSe_2 sub-layer.

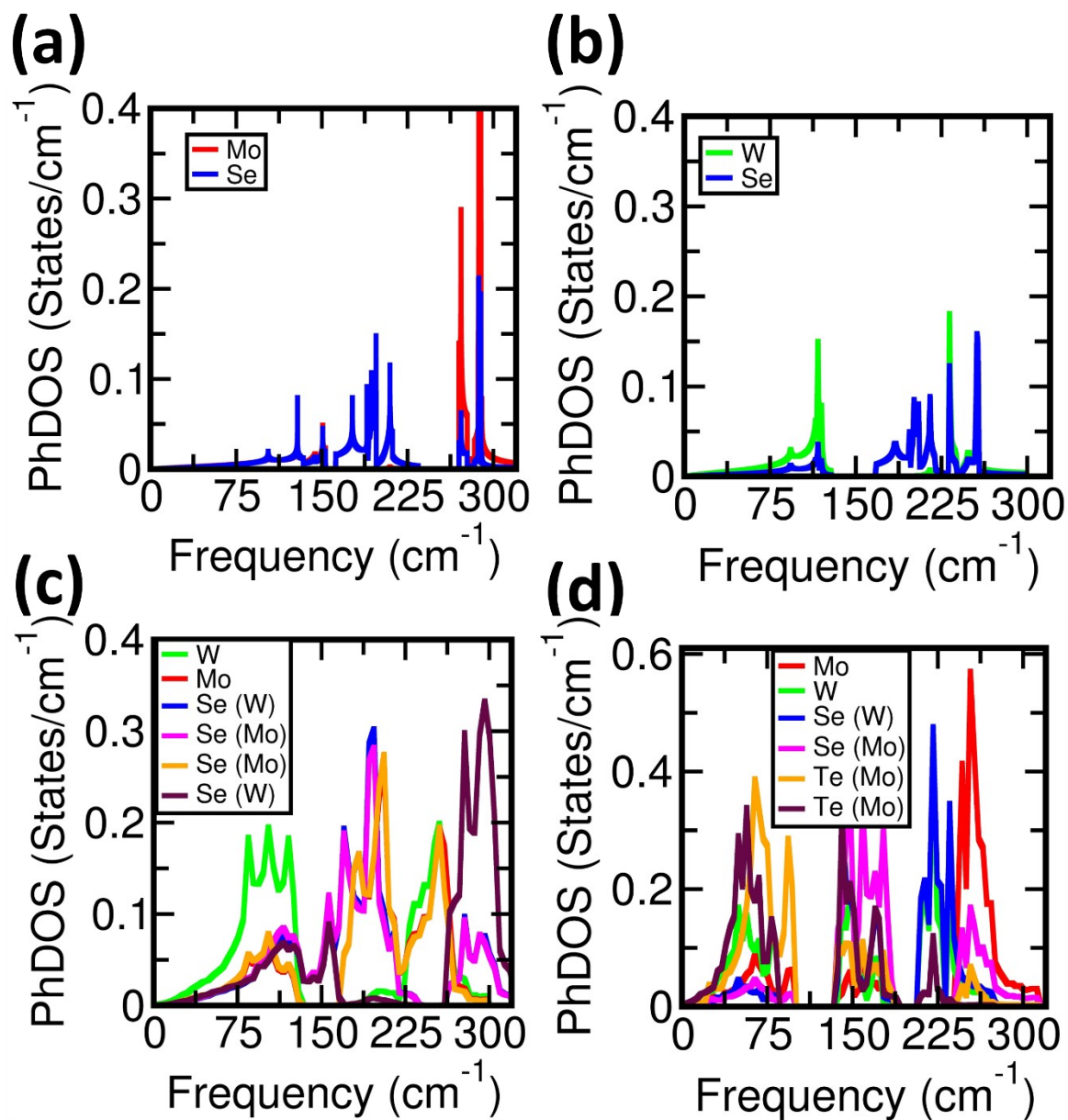


Fig. S3 Phonon density of states as a function of frequency for (a) MoSe₂ and (b) WSe₂ monolayers (c) MoSe₂/WSe₂ and (d) MoSeTe/WSeTe,

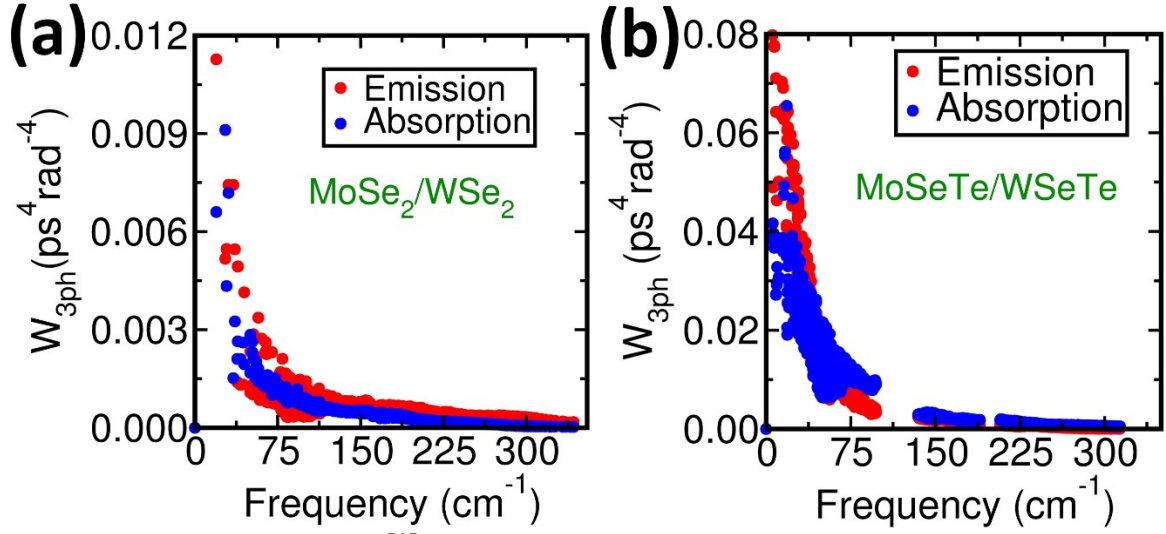


Fig. S4 Weighted phase space (W_{3ph}) as a function of frequency for (a) $\text{MoSe}_2/\text{WSe}_2$ and (b) $\text{MoSeTe}/\text{WSeTe}$ heterostructures, respectively.

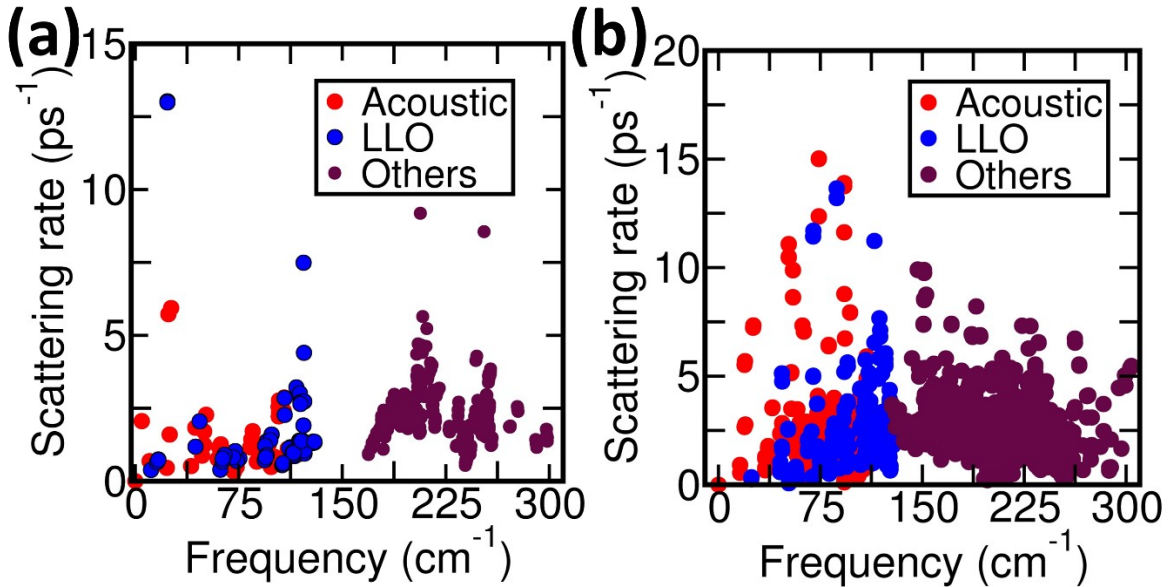


Fig. S5 Anharmonic scattering rates for (a) WSe_2 and (b) $\text{WSe}_2/\text{WTe}_2$ bulk structure, respectively.

Table S5. Lattice thermal conductivity values using iterative, RTA and Slack method as a function of temperatures for (a) $\text{MoSe}_2/\text{WSe}_2$ and (b) $\text{MoSeTe}/\text{WSeTe}$ heterostructures, respectively.

System	Temperature (K)	Iterative (W/mK)	RTA (W/mK)	Slack (W/mK)
$\text{MoSe}_2/\text{WSe}_2$ HS	300	2.83	2.42	4.58
	400	2.14	1.83	3.43

	500	1.72	1.47	2.74
	600	1.44	1.23	2.29
	700	1.24	1.06	1.96
MoSeTe/WSeTe HS	300	0.50	0.14	0.15
	400	0.37	0.10	0.11
	500	0.30	0.085	0.091
	600	0.25	0.074	0.076
	700	0.21	0.065	0.065

2. Electronic structural properties

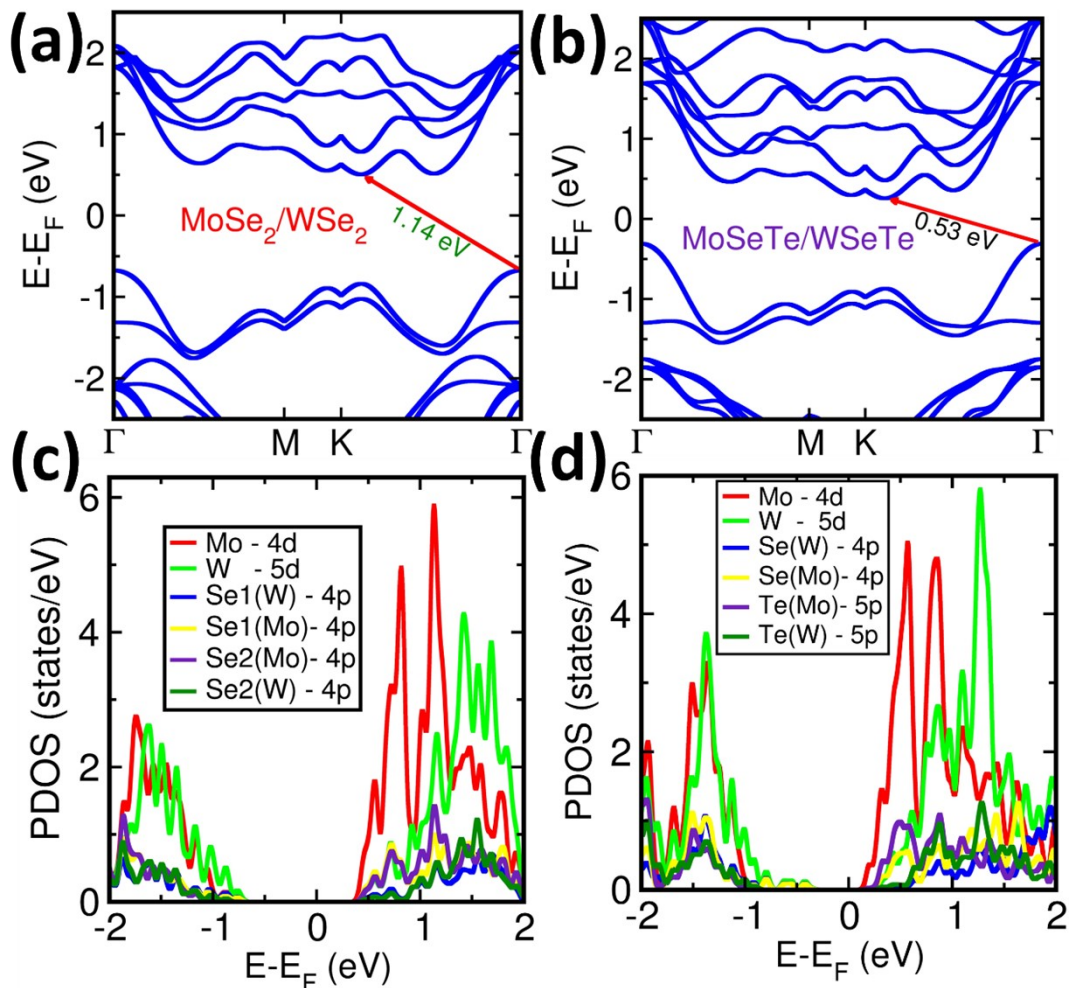


Fig. S6 Electronic band structures of (a) MoSe₂/WSe₂ and (b) MoSeTe/WSeTe heterostructures, along the high symmetry points $\Gamma - M - K - \Gamma$ within the Brillouin zone (BZ). (c) and (d) projected density of states as a function of energy for MoSe₂/WSe₂ and MoSeTe/WSeTe heterostructures, respectively.

To accurately account the electronic properties of the studied heterostructures, we have plotted the electronic band structures of MoSe₂/WSe₂ and MoSeTe/WSeTe heterostructures calculated using PBE method along the high symmetry points $\Gamma - M - K - \Gamma$ within the Brillouin zone (BZ) as illustrated in Fig. S6a and b, respectively. Additionally, we compute the band structures of constituent monolayers (MoSe₂ and WSe₂) shown in Fig. S7 of the SI, closely aligns with the previously reported data^{1,2}. Earlier studies^{1,2,12} demonstrate that the hexagonal phase of 2D MoSe₂ and WSe₂ exhibit a direct band gap, with both conduction band minima (CBM) and valence band maxim (VBM) at high symmetry K point in the BZ. In our present study, the calculated band structures of the parent materials show a similar trend of direct band gap occurring at the high symmetry K point, characterized by band gaps of 1.55 eV and 1.64 eV for MoSe₂ and WSe₂ monolayers, respectively, which are consistent with previously reported values^{2,12}. However, in case of MoSe₂/WSe₂ and MoSeTe/WSeTe heterostructures, the CBM remains at the zone edge K point, while the VBM shifts towards the centre of Brillouin zone Γ , resulting in the emergence of an indirect band gap in the system, consistent with the previously reported MoS₂ bilayer¹³ and MoS₂/WS₂ bilayer heterostructure¹⁴. The MoSe₂/WSe₂ HS shows an indirect band gap of 1.14 eV, closely aligning with the previously reported theoretical value^{2,15}. The reduction in band gap and the transition from direct to an indirect band gap arise from the interlayer coupling in the van der Waals heterostructure.² Furthermore, the MoSeTe/WSeTe HS exhibits an indirect band gap with a notably low value of 0.53 eV, attributed to the substitution of the larger Te atom instead of Se atom.

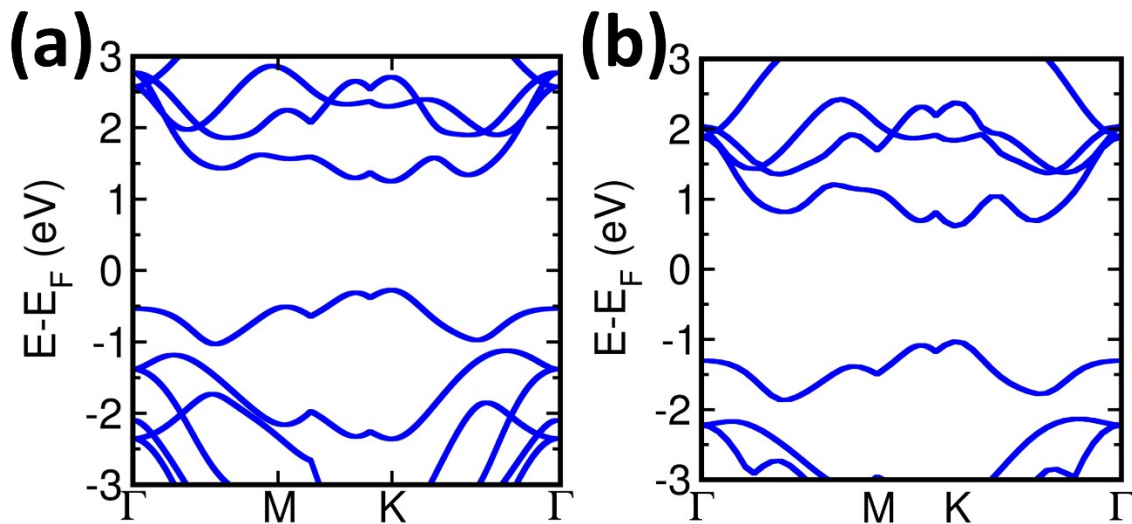


Fig. S7 Electronic band structures for (a) MoSe₂ and (b) WSe₂ monolayers, along the high symmetry points $\Gamma - M - K - \Gamma$ within the Brillouin zone (BZ).

To give a more comprehensive understanding of the layer-wise contributions to the band structure in heterostructures, we plot the projected band structure as depicted in Fig. S8 of the Supporting Information, where the electronic states are projected onto each constituent monolayer. For the MoSe₂/WSe₂ HS, it is clear that the CBM is primarily contributed by the

MoSe₂ sub-layer, whereas the VBM is dominated by the WSe₂ sub-layer. Similarly, in the MoSeTe/WSeTe HS, the CBM is mainly contributed by the MoSeTe sub-layer, while the VBM is predominantly influenced by the WSeTe sub-layer. Henceforth, both heterostructures exhibits type-II band alignment¹⁵, where the CBM is localised in the Mo based layer and the VBM is localised in the W based layer. The layer-wise contribution to the electronic states offers insights into the transport properties of the heterostructures, indicating that the MoSe₂ layer predominately influence the electron transport, while the hole transport is primarily governed by the WSe₂ layer. Additionally, we plot the projected density of states (DOS) as a function of energy, as shown in Fig. S6c and d, to provide insights into the orbital contributions to the band dispersion. In case of MoSe₂/WSe₂ HS, the conduction band (CB) near the Fermi level is predominantly contributed by the 4d (Mo), with a fair contribution from the 4p (Se) atoms associated with Mo atom. Meanwhile, the valence band (VB) near the Fermi level is mainly contributed by the 5d (W), with smaller contributions from the 4p (Se) atoms bonded with W atom. These orbital contributions arising from different atoms further verifies the layer-wise contributions observed in the projected band structure. Furthermore, in MoSeTe/WSeTe HS, the CB near the Fermi level is primarily influenced by the 4d (Mo), with minor contributions from the 4p (Se) and 5p (Te) orbitals connected with Mo atom, respectively. Moreover, the VB near the Fermi level of MoSeTe/WSeTe HS, is dominated by the 5d (W), along with contributions from the 4p (Se) and 5p (Te) orbitals bonded with W atom.

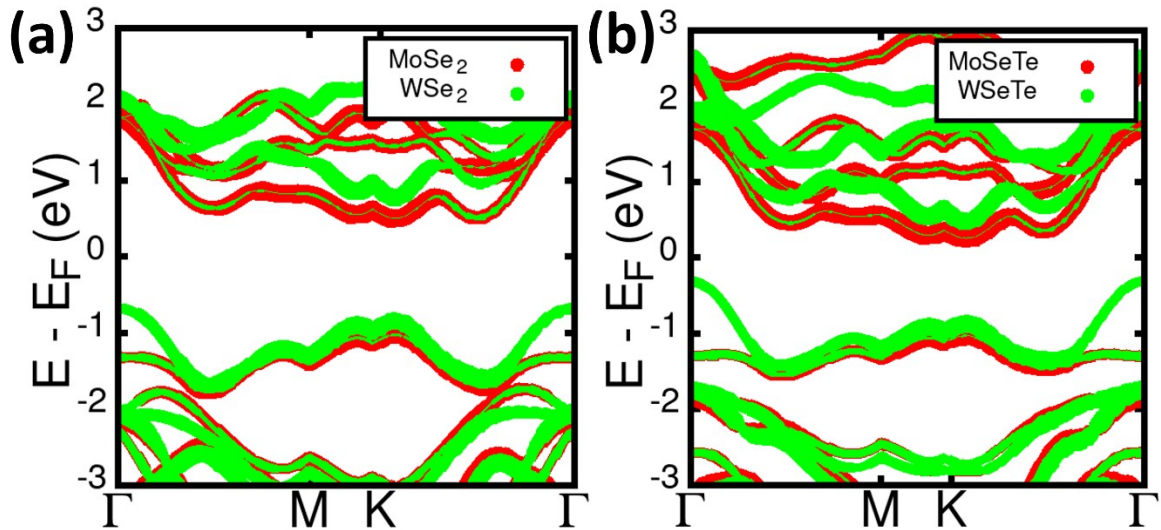


Fig. S8 Projected electronic band structures for (a) MoSe₂/WSe₂ and (b) MoSeTe/WSeTe monolayers, respectively, along the high symmetry points $\Gamma - M - K - \Gamma$ within the Brillouin zone (BZ).

3. Carrier transport formalism

It is well known fact that the scattering between charge carriers (electrons/holes) and acoustic phonons predominates in the low energy region.¹⁶ Therefore, the mobility of carriers in all monolayers is calculated using the deformation potential theory¹⁷, introduced by Bardeen and Shockley in 1950, which accounts the interaction of charge carriers with lattice acoustic

vibrations.¹⁷ Deformation potential theory provides a formula that incorporates the effective mass of carriers to accurately calculate the longitudinal acoustic (LA) phonon-limited mobility in 2D semiconductors given as,^{17,18}

$$\mu_{LA} = \frac{C_{2D} \hbar^3 e}{E_1^2 (m^*)^2 k_B T} \quad (1)$$

Where μ is the mobility of charge carriers, C_{2D} is the elastic constant, \hbar is the reduced Planck constant, e is the electronic charge, E_1 is the deformation potential constant, m^* is the carrier effective mass, k_B is the Boltzmann constant and T is the temperature. Effective mass (m^*) of charge carrier is related to the curvature of the energy band in $E - K$ diagram in the reciprocal

space, determined using the equation given as¹⁸, $m^* = \hbar^2 \left[\frac{d^2 E_k}{dk^2} \right]^{-1}$. The deformation potential constant or carrier-phonon scattering strength (E_1) represents the energy shift observed in the band edge position due to the application of uniaxial strain. It is determined by performing a linear fitting analysis of band edge positions of the conduction band minima (CBM) and valence band maxima (VBM) as a function of lattice deformation induced by uniaxial strain.

The uniaxial strain is calculated using the equation derived as,¹⁸ $\epsilon = \frac{a - a_o}{a_o}$, where ϵ is the applied uniaxial strain, a_o is the actual lattice parameter and a denotes the lattice parameter after the application of uniaxial strain. On the other hand, elastic constant C_{2D} is derived as¹⁸, $2(E - E_o) = C_{2D} S_o \left(\frac{\Delta a}{a_o} \right)^2$, where E_o and S_o represents the total energy and lattice cross sectional area of the unit cell in the absence of strain, respectively. Additionally, E denotes the total energy of the system under the influence of applied uniaxial strain.

Table S6. Calculated values of elastic constant (C_{2D}), deformation potential constant (E_1), carrier effective mass (m^*), acoustic phonon limited carrier mobility (μ_{LA}) and relaxation time (τ) [$m_o = 9.1 \times 10^{-31}$ Kg] at 300 K.

System	e/h	C_{2D} (J/m ²)	E_1 (eV)	m^* (m_o)	μ_{LA} (cm ² V ⁻¹ s ⁻¹)	$\tau \times 10^{-12}$ (s)
MoSe ₂ ¹⁹	CB	124.20	6.24	0.55	1072.90	0.33
	VB		1.76	0.71	578.30	0.23
WSe ₂ ²	CB	70.46	2.14	0.13	16925.00	1.33

	VB		6.56	0.34	296.50	0.05
MoSe₂/WSe₂ HS	CB	850.53	2.71	0.22	49157.20	6.15
	VB		4.66	0.27	11030.29	1.69
MoSeTe/WSeTe HS	CB	1600.02	2.58	0.23	93664.03	12.25
	VB		7.36	0.20	15236.84	1.73

Table S7. Area (A), thickness (t) dielectric constant (ϵ), Bose Einstein distribution (n) and Born-effective charge (Z_{MB}) are tabulated.

System	A $\times 10^{-25}$ (m²)	t $\times 10^{-10}$ m	ϵ	n	Z_{MB}
MoSe₂	28.67	3.35	16.14	0.86	1.75
WSe₂	28.75	3.36	13.26	0.82	1.12
MoSeTe	31.25	3.47	18.87	1.14	2.47
WSeTe	30.97	3.35	17.18	1.08	1.82

Table S8. p - type and n - type Seebeck coefficient values as a function of temperatures for (a) MoSe₂/WSe₂ and (b) MoSeTe/WSeTe heterostructures.

System	Temperature (K)	Seebeck coefficient ($\mu V/K$)	
		p- type	n- type
MoSe₂/WSe₂ HS	300	1302.52	1316.53
	400	993.69	981.09
	500	805.95	777.38
	600	691.17	647.05
	700	600.77	550.84
MoSeTe/WSeTe HS	300	612.74	671.56
	400	442.99	519.88
	500	331.30	434.45
	600	261.27	378.43
	700	212.25	339.21

Reference

- 1 S. Kumar and U. Schwingenschlög, *Chem. Mater.*, 2015, **27**, 1278–1284.
- 2 B. Amin, N. Singh and U. Schwingenschlög, *Phys. Rev. B*, 2015, **92**, 075439.
- 3 X. Zhao, G. Tang, Y. Li, M. Zhang and Y. Nie, *ACS Appl. Electron. Mater.*, 2021, **3**, 2995–3004.
- 4 R. C. Andrew, R. E. Mapasha, A. M. Ukpogon and N. Chetty, *Phys. Rev. B*, 2012, **85**, 125428.

- 5 R. Hill, *Proceedings of the Physical Society. Section A*, 1952, **65**, 349.
- 6 D. Çakır, F. M. Peeters and C. Sevik, *Appl. Phys. Lett.*, 2014, **104**, 203110.
- 7 H. Sun, P. Agrawal and C. V. Singh, *Mater. Adv.* 2021, **2**, 6631–6640.
- 8 C. J. Price and S. P. Hepplestone, *J. Mater. Chem. C*, 2023, **11**, 14278–14291.
- 9 M. A. Blanco, J. M. Recio, A. Costales and R. Pandey, *Phys. Rev. B*, 2000, **62**, R10599–R10602.
- 10 P. Liu, Y. Zhao, J. Ni and Z. Dai, *Phys. Rev. Appl.*, 2024, **22**, 034049.
- 11 K. Pal, Y. Xia, J. He and C. Wolverton, *Phys. Rev. Mater.*, 2019, **3**, 085402.
- 12 G. Özbal, R. T. Senger, C. Sevik and H. Sevinçli, *Phys. Rev. B*, 2019, **100**, 085415.
- 13 T. Cheiwchanamngij and W. R. L. Lambrecht, *Phys. Rev. B*, 2012, **85**, 205302.
- 14 W. Zhang, A. Srivastava, X. Li and L. Zhang, *Phys. Rev. B*, 2020, **102**, 174301.
- 15 O. Garrity, T. Brumme, A. Bergmann, T. Korn, P. Kusch and S. Reich, *Nano Lett.*, 2024, **24**, 11853-11858.
- 16 D. Han, X. Yang, M. Du, G. Xin, J. Zhang, X. Wang, L. Cheng, *Nanoscale*, 2021, **13**, 7176–7192.
- 17 J. Bardeen and W. Shockley, *Phys. Rev.* 1950, **80**, 72–80.
- 18 A. Shafique, A. Samad and Y. H. Shin, *Phys. Chem. Chem. Phys.*, 2017, **19**, 20677–20683.
- 19 L. Cheng and Y. Liu, *J. Am. Chem. Soc.*, 2018, **140**, 17895–17900.